Received 18 July 2022; revised 26 August 2022; accepted 17 September 2022. Date of publication 26 September 2022; date of current version 7 October 2022.

Digital Object Identifier 10.1109/OJCOMS.2022.3209641

An Experimental Proof of Concept for Integrated Sensing and Communications Waveform Design

TONGYANG XU [1,2] (Member, IEEE), FAN LIU [3] (Member, IEEE), CHRISTOS MASOUROS [2] (Senior Member, IEEE), AND IZZAT DARWAZEH [2] (Senior Member, IEEE)

[1]School of Engineering, Newcastle University, NE1 7RU Newcastle upon Tyne, U.K.

[2]Department of Electronic and Electrical Engineering, University College London, WC1E 7JE London, U.K.

[3]Department of Electronic and Electrical Engineering, Southern University of Science and Technology, Shenzhen 518005, China

CORRESPONDING AUTHOR: T. XU (e-mail: tongyang.xu@ieee.org)

This work was supported by the Engineering and Physical Sciences Research Council (EPSRC) General under Grant EP/S028455/1.

ABSTRACT The integration of sensing and communication (ISAC) functionalities have recently gained significant research interest as a hardware-, power-, spectrum- and cost- efficient solution. This experimental work implements a dual-functional sensing and communication framework where a single radiation waveform, either omnidirectional or directional, can realize both sensing and communication functions. We design an orthogonal frequency division multiplexing (OFDM) based multi-user multiple input multiple output (MIMO) software-defined radio (SDR) testbed to validate the dual-functional model. We carry out over-the-air experiments to investigate the optimal trade-off factor to balance the performance for both functions. On the communication side, we obtain bit error rate (BER) results from the testbed to show the communication performance using the dual-functional waveform. On the sensing performance, we measure the output beampatterns of our transmission to examine their similarity to simulation based beampatterns. We also implement a sensing experiment to realize activity detection functions. Our experiment reveals that the dual-functional approach can achieve comparable BER performance with pure communication-based solutions while achieving fine sensing beampatterns and realistic sensing functionality simultaneously.

INDEX TERMS Waveform, communications, sensing, integrated sensing and communications (ISAC), OFDM, MIMO, software-defined radio (SDR), over-the-air, prototyping.

I. INTRODUCTION

WIRELESS communications have evolved from 1G to 5G with significant technology innovations. Traditionally, signals are transmitted at low-frequency carriers with narrow signal bandwidth due to limitations from hardware and technical theories. Nowadays, signals can be transmitted at millimeter wave (mmWave) frequency [1] and TeraHertz (THz) frequency [2] with GHz signal bandwidth. In terms of antennas, communication systems can integrate hundreds of antennas in massive multiple input multiple output (MIMO) [3]. Moreover, in terms of signal waveform, different options are available such as code division multiple access (CDMA) in 3G [4], orthogonal frequency division multiplexing (OFDM) and single carrier frequency division multiple access (SC-FDMA) in 4G/5G [5], [6]. Recently, advanced waveform candidates are being investigated for future 6G such as spectrally efficient frequency division multiplexing (SEFDM) [7], faster than Nyquist (FTN) [8], [9], orthogonal time frequency space (OTFS) [10], [11], generalized frequency division multiplexing (GFDM) [12] and filter bank multicarrier (FBMC) [13].

Complementary to wireless communications, various sensors have been used to sense the world such as accelerometers, Gyroscope, light sensor, temperature sensors, audio and video. Due to the ubiquitous features of wireless signals, smart applications such as non-intrusive and non-contact radar sensing and radio frequency (RF) sensing are becoming popular. In [14], Google develops a mmWave radar sensing system at 60 GHz termed 'Soli', which can sense and understand subtle motions in finger gestures. Work in [15] tests different radar and sonar devices for detecting different classes of mobility via measuring micro-Doppler [16] sensitivity.

In [17], a joint detection system that integrates a camera with an frequency-modulated continuous wave (FMCW) radar is designed to realize object detection and 3D estimation. In [18], a ultra-wideband (UWB) MIMO radar equipped with manufactured Vivaldi antennas is designed and implemented to detect objects behind walls using stepped-frequency continuous wave (SFCW) signals. Moreover, the variations of reflected signals can judge human motions even behind walls. The representative work is [19], where a special method, termed inverse synthetic aperture radar (ISAR), is applied to deal with a moving object using a single receiver antenna. Recently, an IEEE group is working on an IEEE 802.11bf standard [20], which aims to use existing wireless fidelity (WiFi) signals to realize sensing functions. There are commonly two methods for estimating human activities based on WiFi signals, namely received signal strength indicator (RSSI) [21], [22], [23], [24] and channel state information (CSI) [25]. Although RSSI has been successful in human activity detections, its coarse sensing resolution and high sensitivity to noise limit its applications in further areas. The second solution, CSI, aims to extract amplitude [26] and phase information [27], [28] to better assist human activity detections. In [29], a WiFall system is designed to 'see' human activities via measuring CSI. A detailed propagation model is analytically studied to reveal the possibility of detecting human fall activities. In [30], a WiHear system is designed to 'hear' human talks based on micro-movement via radio reflections from mouth movements. In [31], CSI information is extracted from both OFDM signals and MIMO antennas. Therefore, detection accuracy is improved. In [32], CSI from WiFi signals is extracted for monitoring vital signs and postures during sleeping.

It is noted that traditional sensing signals are not initially designed for communications. Conversely, signalling for communications is not inherently designed to serve sensing functionalities. To achieve the joint sensing and communication purpose, communication radio signals and sensing signals have to be managed in time division multiplexing (TDM) mode, frequency division multiplexing (FDM) mode or space division multiplexing (SDM) mode. However, the multiplexing strategy will waste time, frequency or spatial resources. A number of approaches have emerged, aiming to design and test signalling that is appropriate for integrated sensing and communication (ISAC). Work in [33] proposed to use primary synchronization signal (PSS) in the LTE frame for the radar sensing purpose. Work in [34] proposed a space division multiple access (SDMA) scheme that can support radar and communications using the same transmit hardware with the same timing and spectral occupation. The principle behind the work is to send spatially orthogonal beams at the null space of the other one. Therefore, interference is avoided. This was further demonstrated experimentally in [35], where analog-domain phased array antennas were employed to assist radar beam tracking and alignment. Work in [36] studied a new waveform design in ISAC. The principle is to multiplex low out-of-band power emission signals with radar signals in frequency domain. However, this is a frequency multiplexing scheme and is not a dual-functional design. In addition, its experiment is based on single-antenna point to point links. Work in [37] proposed to use mutually orthogonal waveforms via space time coding (STC) in different beams for communication and radar rather than a single waveform beam. Work in [38] aims to realize joint communication and radar functions in an FDM mode via full-duplex in hardware based solutions. Work in [39] designs a joint communication-radar experiment using single-carrier signals in a TDM mode via full-duplex radar reception. Work in [40] proposed to achieve joint communication and radar functions by modulating information signalling onto standard radar waveforms through index modulation.

The main contribution of this work is to practically design and test over the air a dual-functional waveform [41] for an integrated sensing and multi-user MIMO-OFDM communication system [42]. In general, there are three categories of ISAC waveform designs [43] namely, pure-sensing, pure-communication, and joint sensing-communication design. The first type is to integrate communication data into existing sensing waveforms, which may result in limited communication rate. The second type is to utilize existing standard compatible communication waveforms to sense a target directly, which might suffer from poor sensing performance, as the waveform is not tailored for sensing. The third type is to achieve a balanced trade-off between sensing and communication such as the work in [41]. Unlike existing experimental work in pure-sensing signal or pure-communication signal design, the prototyping testbed in this paper can realize sensing and communication using the same time, frequency and spatial resources. As a step ahead from [41], the designed dual-functional ISAC experiment in this work is based on the OFDM signal waveform, which enables a straightforward deployment of the ISAC framework in many standard communication systems. Additionally, unlike pure theoretical simulations, this work obtains a practically working sensing and communication trade-off factor that ensures sensing beampattern quality and communication performance after comprehensive experiments on communication constellation diagrams, bit error rate (BER), error vector magnitude (EVM), sensing beampattern quality and sensing detection accuracy. Based on both communication performance and sensing performance, this work validates the dual functionality of the proposed ISAC transmission scheme in real world.

The rest of this paper is organized as follows. Section II will introduce the fundamentals of signal waveforms and multi-antenna communication architectures. In Section IV, the trade-off between sensing and communication is explained using the ISAC model, followed by the beampattern illustrations in pure sensing and pure communication systems. A multi-user MIMO-OFDM experiment is designed and implemented in Section V to verify the ISAC framework in hardware. Finally, Section VII concludes the work.

II. COMMUNICATION MODEL

We consider a multi-user MIMO-OFDM transmission, for which the received signal can be expressed as

$$\mathbf{Y} = \mathbf{H}\tilde{\mathbf{X}} + \mathbf{W}, \tag{1}$$

where $\mathbf{Y} = [\mathbf{y}_1, \mathbf{y}_2, \ldots, \mathbf{y}_K]^T \in \mathbb{C}^{K\times L}$ indicates K parallel sample vectors for K receiver side users with L samples per user. $\mathbf{H} = [\mathbf{h}_1, \mathbf{h}_2, \ldots, \mathbf{h}_K]^T \in \mathbb{C}^{K\times N}$ indicates a MIMO channel matrix with N being the number of transmitter side antennas. $\tilde{\mathbf{X}} = [\tilde{\mathbf{x}}_1, \tilde{\mathbf{x}}_2, \ldots, \tilde{\mathbf{x}}_N]^T \in \mathbb{C}^{N\times L}$ is the transmission symbol matrix after precoding, with L being the number of time samples per data stream on each antenna. Similarly, the noise matrix $\mathbf{W} = [\mathbf{w}_1, \mathbf{w}_2, \ldots, \mathbf{w}_K]^T \in \mathbb{C}^{K\times L}$ indicates K parallel noise vectors for K receiver side users with L noise samples per user.

The commonly used multicarrier signal format in 4G, 5G and WiFi standards is OFDM, which we employ in this work. Traditionally, each antenna is responsible for an OFDM symbol stream. Therefore, the symbol transmission matrix consists of N parallel OFDM data streams with L time samples for each data stream. The expression in (1) can be rewritten as

$$\mathbf{Y} = \mathbf{X} + \underbrace{\left(\mathbf{H}\tilde{\mathbf{X}} - \mathbf{X}\right)}_{MUI} + \mathbf{W}, \tag{2}$$

where $\mathbf{X} = [\mathbf{x}_1, \mathbf{x}_2, \ldots, \mathbf{x}_K]^T \in \mathbb{C}^{K\times L}$ indicates the user side multicarrier symbol matrix. The term within the bracket in (2) represents multi-user interference (MUI) and the total power contributed by the MUI term is therefore computed as

$$P_{MUI} = \left\|\mathbf{H}\tilde{\mathbf{X}} - \mathbf{X}\right\|_F^2, \tag{3}$$

where $\|\cdot\|_F$ denotes the Frobenius matrix norm. The value of P_{MUI} is determined by the quality of precoding. In order to minimize the value of P_{MUI}, we should optimize $\tilde{\mathbf{X}}$ such that its multiplication with the channel $\mathbf{H}$ leads to a result close to $\mathbf{X}$.

An OFDM signal with Q time samples is expressed as

$$x_k = \frac{1}{\sqrt{Q}} \sum_{m=1}^{M} s_m \exp\left(\frac{j2\pi mk}{Q}\right), \tag{4}$$

where x_k is the k^{th} time sample with the index of $k = 1, 2, \ldots, Q$, M is the number of sub-carriers, $Q = \rho M$ indicates the number of time samples and ρ is the oversampling factor. $\frac{1}{\sqrt{Q}}$ is the normalization factor and s_m is the m^{th} single-carrier symbol in one OFDM symbol.

A matrix format can convert the expression in (4) to the following

$$\mathbf{x} = \mathbf{F}\mathbf{s}, \tag{5}$$

where $\mathbf{x} \in \mathbb{C}^{Q\times 1}$ is an OFDM symbol vector within $\mathbf{X} = [\mathbf{x}_1, \mathbf{x}_2, \ldots, \mathbf{x}_K]^T$, $\mathbf{F} \in \mathbb{C}^{Q\times M}$ indicates a sub-carrier matrix with elements noted as $\exp(\frac{j2\pi mk}{Q})$ and $\mathbf{s} \in \mathbb{C}^{M\times 1}$ indicates the symbol vector. The received signal, assuming perfect precoding, is expressed as

$$\mathbf{y} = \mathbf{F}\mathbf{s} + \mathbf{w}, \tag{6}$$

where $\mathbf{y} \in \mathbb{C}^{Q\times 1}$ indicates one OFDM symbol at one receiver side user. For an OFDM frame, we need multiple OFDM symbols with overall $L = Q \times \psi$ time samples, where ψ indicates the number of OFDM symbols. Moreover, in order to support a MIMO system defined in (1), we need to generate N parallel OFDM signal streams. In the following, we will discuss the methodology of precoding $\mathbf{X} \in \mathbb{C}^{K\times L}$ to the dual-functional sensing and communication waveform $\tilde{\mathbf{X}} \in \mathbb{C}^{N\times L}$.

III. SENSING MODEL

Unlike traditional analog phased-array radar sensing systems, digital MIMO radar systems have higher degree of freedom (DoF) due to the use of uncorrelated waveforms. The design of such a MIMO waveform is equivalent to the design of the covariance matrix [44] of probing signals, where convex optimization might be used. The spatial covariance matrix of $\tilde{\mathbf{X}}$ has the following expression

$$\mathbf{R}_d = \frac{1}{L}\tilde{\mathbf{X}}\tilde{\mathbf{X}}^H, \tag{7}$$

where $\mathbf{R}_d$ determines the sensing beampattern and it should be positive-definite and $L \geq N$.

To achieve the dual-functional sensing and communications, we need to optimize the transmission symbol matrix $\tilde{\mathbf{X}}$, which can minimize P_{MUI} in (3) considering multi-antenna and multicarrier signals, and simultaneously meet the MIMO radar constraints in (7).

In general, there are two types of MIMO radar sensing waveform designs. One is the orthogonal waveform, which generates omni-directional beampattern for searching unknown targets. Alternatively, MIMO radar may also track known targets via directional waveforms [45]. Without loss of generality, in this paper we show that the proposed approach is capable of designing both orthogonal and directional MIMO radar waveforms while carrying communication information, which will be validated by experimental results.

In order to get an omnidirectional beampattern, the transmission waveform matrix $\tilde{\mathbf{X}}$ has to be orthogonal such that its corresponding covariance matrix is an identity matrix. The optimization problem is formulated as

$$\begin{aligned} \min_{\tilde{\mathbf{X}}} \quad & \left\|\mathbf{H}\tilde{\mathbf{X}} - \mathbf{X}\right\|_F^2 \\ \text{s.t.} \quad & \frac{1}{L}\tilde{\mathbf{X}}\tilde{\mathbf{X}}^H = \frac{P_T}{N}\mathbf{I}_N \end{aligned} \tag{8}$$

where P_T indicates the total transmission power and $\mathbf{I}_N$ is an $N \times N$ identity matrix.

For a directional MIMO radar beampattern, a unique covariance matrix $\mathbf{R}_d$ is considered in the MUI optimization

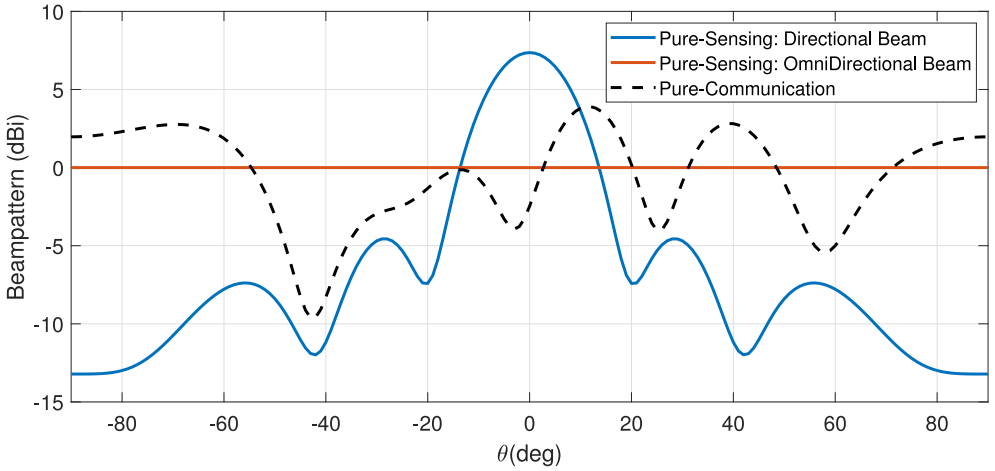

FIGURE 1. Spatial beampattern illustration for pure-communication (γ=1) and pure-sensing (γ=0) when considering a MIMO-OFDM ISAC system with six transmission antennas.

problem as

$$\begin{aligned} \min_{\tilde{\mathbf{X}}} \quad & \left\|\mathbf{H}\tilde{\mathbf{X}} - \mathbf{X}\right\|_F^2 \\ \text{s.t.} \quad & \frac{1}{L}\tilde{\mathbf{X}}\tilde{\mathbf{X}}^H = \mathbf{R}_d, \end{aligned} \tag{9}$$

where $\mathbf{R}_d$ is positive-definite and we refer readers to [44] for the specific design methodology.

IV. TRADE-OFF BETWEEN SENSING AND COMMUNICATIONS

To realize a dual-functional sensing communication function, we employ the optimization methodology from [41] where a trade-off factor γ is introduced to balance the performance of the communication part and the sensing part. In this case, the resulting waveform can provide a balanced solution to both communication and sensing functions.

We define the desired sensing signal as $\mathbf{X}_d$ where its design is detailed in [44]. The trade-off optimization problem considering the total power constraint is formulated as

$$\begin{aligned} \min_{\tilde{\mathbf{X}}} \quad & \gamma\left\|\mathbf{H}\tilde{\mathbf{X}} - \mathbf{X}\right\|_F^2 + (1-\gamma)\left\|\tilde{\mathbf{X}} - \mathbf{X}_d\right\|_F^2 \\ \text{s.t.} \quad & \frac{1}{L}\left\|\tilde{\mathbf{X}}\right\|_F^2 = P_T, \end{aligned} \tag{10}$$

where the first term, $\|\mathbf{H}\tilde{\mathbf{X}} - \mathbf{X}\|_F^2$ aims to minimize the MUI while the second term $\|\tilde{\mathbf{X}} - \mathbf{X}_d\|_F^2$ aims to enforce the signal waveform to approach the desired sensing waveform $\mathbf{X}_d$. $0 \le \gamma \le 1$ indicates the trade-off factor that balances the communication and sensing performance.

We can expand the two Frobenius norms and combine them in a single norm format as

$$\begin{aligned} &\gamma\left\|\mathbf{H}\tilde{\mathbf{X}} - \mathbf{X}\right\|_F^2 + (1-\gamma)\left\|\tilde{\mathbf{X}} - \mathbf{X}_d\right\|_F^2 \\ &= \left\|\left[\sqrt{\gamma}\mathbf{H}^T, \sqrt{1-\gamma}\mathbf{I}_N\right]^T\tilde{\mathbf{X}} - \left[\sqrt{\gamma}\mathbf{X}^T, \sqrt{1-\gamma}\mathbf{X}_d^T\right]^T\right\|_F^2. \end{aligned} \tag{11}$$

To simplify the expression, we define $\mathbf{A} = [\sqrt{\gamma}\mathbf{H}^T, \sqrt{1-\gamma}\mathbf{I}_N]^T \in \mathbb{C}^{(K+N)\times N}$, $\mathbf{B} = [\sqrt{\gamma}\mathbf{X}^T, \sqrt{1-\gamma}\mathbf{X}_d^T]^T \in \mathbb{C}^{(K+N)\times L}$. Therefore, (10) can be reformulated as

$$\begin{aligned} \min_{\tilde{\mathbf{X}}} \quad & \left\|\mathbf{A}\tilde{\mathbf{X}} - \mathbf{B}\right\|_F^2 \\ \text{s.t.} \quad & \left\|\tilde{\mathbf{X}}\right\|_F^2 = LP_T. \end{aligned} \tag{12}$$

While problem (12) is non-convex due to the quadratic equality constraint, it can be proved that strong duality holds, such that (12) can be optimally solved via solving the dual problem [41]. To reduce the complexity incurred by the iterative algorithm of solving the dual problem, we consider a closed-form sub-optimal solution, which is obtained by using the simple least squares (LS) method under the total power constraint as the following

$$\tilde{\mathbf{X}} = \frac{\sqrt{LP_T}}{\left\|\mathbf{A}^\dagger\mathbf{B}\right\|_F}\mathbf{A}^\dagger\mathbf{B}, \tag{13}$$

where $(\cdot)^\dagger$ represents the pseudo inverse of the matrix.

The trade-off performance for pure communication systems ($\gamma = 1$) and pure sensing systems ($\gamma = 0$) are demonstrated in Fig. 1. It is obvious from (10) that when the trade-off factor $\gamma = 0$, the intended waveform will match closely the perfect sensing waveform as shown in Fig. 1 while it will be far away from the communication featured waveform. In this case, the scenarios with $\gamma = 0$ would cause performance degradation in communications. When the trade-off factor is increased to $\gamma = 1$, the sensing part in (10) will be removed. Therefore, the communication part dominates the integrated system and the intended waveform will be more likely to follow the optimal communication constraints. In this case, $\gamma = 1$ leads to pure communication functionality and Fig. 1 reveals that the 'Pure-Communication' sensing beampattern is more likely to be random, which is far away from 'Pure-Sensing' omnidirectional and directional beampatterns.

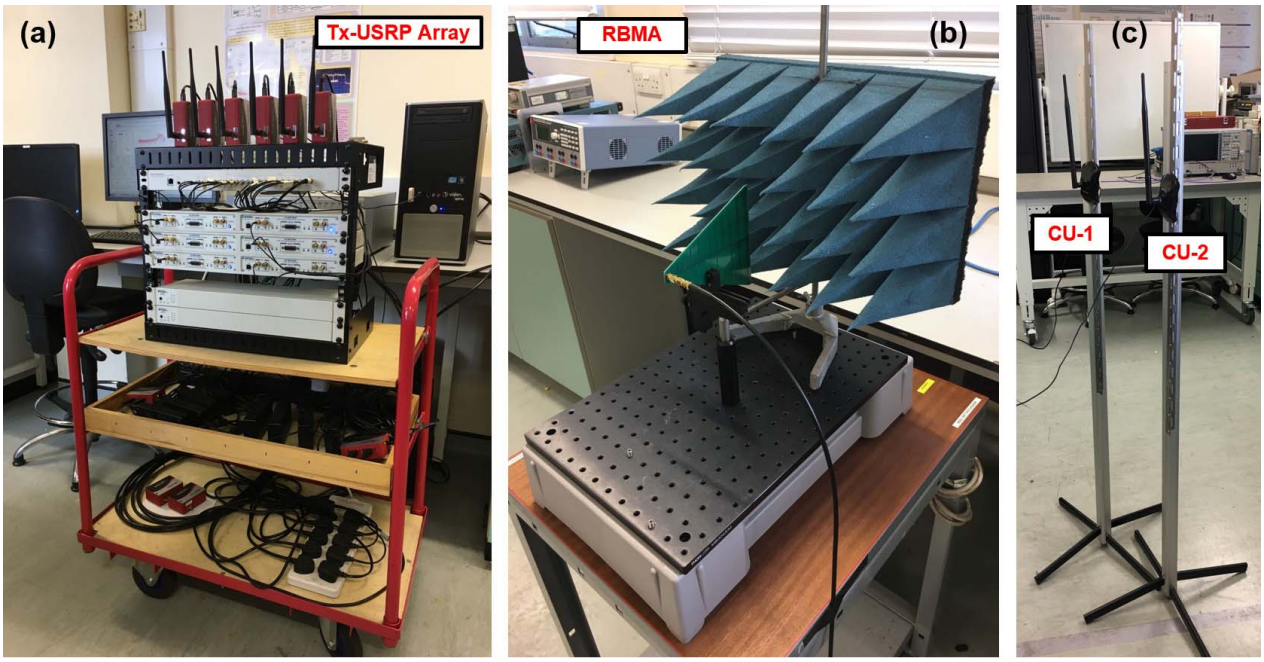

FIGURE 2. Experiment platform setup. (a) Tx-USRP Array: MIMO transceiver that precodes and decodes multi-user signals. (b) Radar Beampattern Measurement Apparatus (RBMA): a directional antenna to measure beampatterns. (c) CU-1 and CU-2: two omnidirectional antennas to receive communication signals.

For other values of γ, trade-off exists between communication and sensing performance. Explicitly, as γ is increased, priority is given to communications at the expense of sensing performance, and vice versa. It is noted that the existence of the trade-off factor cannot ensure optimal performance for both sensing and communication. The advantage of the trade-off is that we can flexibly tune the performance between communication and sensing according to specific application scenarios. Fig. 1 merely shows the general design principle. The variations of communication BER and radar sensing beampattern at different values of γ will be investigated using our experiment testbed in the following sections.

V. EXPERIMENT SETUP AND VALIDATION

A. EXPERIMENT PLATFORM SETUP

As demonstrated in Fig. 2, the designed 6×2 MIMO-OFDM platform is equipped with N=6 transmitter antennas and K=2 users working at 2.4 GHz carrier frequency, consisting of a Tx-USRP array (USRP cluster with antenna array), two communication users (each user is equipped with one antenna and no beamforming at the receiver side), a radar beampattern measurement apparatus (an antenna is connected to a stand-alone RF chain in one of the USRPs of the Tx-USRP array).

1) TX-USRP ARRAY

The emulated base station, noted as the Tx-USRP array, consists of six USRP-RIO-2953R. Each of the devices has two RF chains, in which one can be used for signal generation and the other one is for signal reception. In this experiment, we use one RF chain from each USRP for signal generation at the carrier frequency f_{RF}=2.4 GHz with the sampling rate of 20 MS/s. The symbol modulated at each sub-carrier is QPSK. The number of data sub-carriers is 12 and the inverse fast Fourier transform (IFFT) size is 128. In addition, each OFDM symbol also considers 10 cyclic prefix (CP) samples for the mitigation of channel effects. The output from each USRP is fed to an omnidirectional antenna via a Vaunix LPS-402 programmable phase shifter [46]. In this experiment, the phase shifter is merely used for holding the omnidirectional antenna without any phase control functions. However, the activation of the phase control function in each phase shifter will enable a more power efficient hybrid analog-digital multi-user MIMO system design [47], which could be the future research direction of ISAC. In total, six antennas are placed in a uniform linear array (ULA) format at the top of the testbed with the spacing of half wavelength. As mentioned, the second RF chain in each USRP can be reserved for signal reception. Therefore, the experiment platform can support up to a 6×6 MIMO-OFDM system.

2) COMMUNICATION USERS (CUS)

In this experiment, for simplicity we emulate two users as the receiver side. Therefore, the communication part is a 6×2 MIMO-OFDM system, which includes the Tx-USRP array base station and two CUs at the receiver side. Each CU, equipped with an omnidirectional antenna, is connected to a USRP, which can separately process received signals.

3) RADAR BEAMPATTERN MEASUREMENT APPARATUS (RBMA)

Due to restricted measurement environment, the entire experiment is managed in an indoor laboratory and the

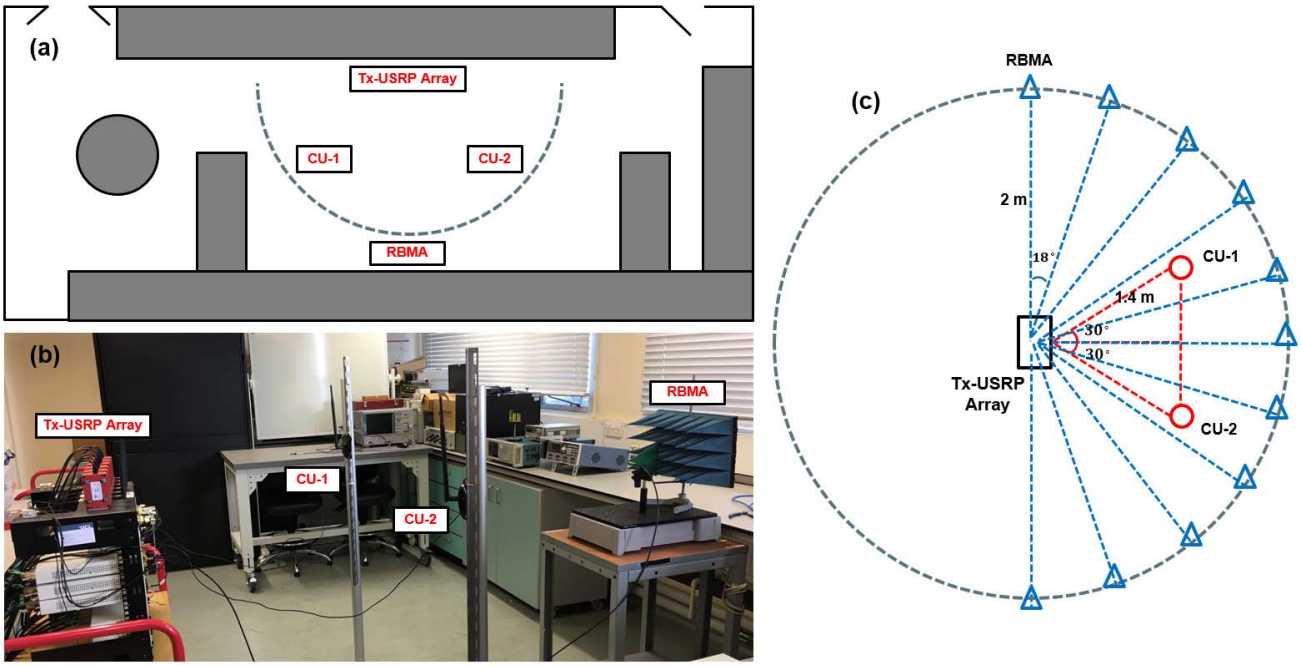

FIGURE 3. Experiment measurement setup. (a) Laboratory floor plan. (b) Platform units arrangement. (c) Beampattern measurement strategy.

line-of-sight (LOS) channel model ensures the signal power from each antenna is sufficiently high. The beampattern measurement will be affected due to signal reflections in such a small indoor space. Nevertheless, measuring the beampattern in an anechoic chamber would significantly hamper our ability to investigate the multipath effects in the performance of the CUs. Therefore, we carried out the experiment in the indoor laboratory to allow rich multipath propagation. For the sensing part, to maximally mitigate the multipath effect, obtain an accurate measurement of the LoS power, and emperically measure the transmitted beampattern, we employ a directional 6 dBi log-periodic (LP) PCB antenna, which works from 850 MHz to 6.5 GHz carrier frequency. To further reduce reflections that would cause pattern measurement errors, we also place radiation absorbing material (RAM) behind the LP antenna. The RAM can efficiently reduce signal reflections with central frequency from 1 GHz to 40 GHz.

B. EXPERIMENT MEASUREMENT SETUP

The floor plan of the experiment setup is shown in Fig. 3(a), where the indoor laboratory is approximately 4 m wide and 9 m long. There are plenty of objects that could cause signal reflection and blocking. For the communication part, this is not an issue since wireless channel will be measured in real time and precoding will be applied correspondingly to mitigate the MIMO transmission interference. Moreover, this experiment employs OFDM signals instead of single-carrier signals. Therefore, the multicarrier structure of OFDM signals is robust to multipath channel effect. Commonly, pilot symbols are used to estimate CSI, which will be used to equalize channel effects using a one-tap equalizer.

The three-dimensional platform setup for the communication part is the following. The location for the Tx-USRP Array and CUs are labelled in Fig. 3(b) where two users are placed in front of the base station. The horizontal distance between two users is 1.4 m and each user is 1.4 m away from the base station. Due to the limited space, to obtain sufficient measurement at various signal-to-noise ratio (SNR), we will maintain the total signal transmission power while adjusting noise for each measurement. To have a flexible and precise control of SNR, we add noise at the receiver side using software. Therefore, we measure received SNR at the user side. The antenna array at the base station is 1.5 m above the floor and the two users are placed 1.5 m above the floor as well. For the beampattern measurement antenna, it is placed 2 m away from the base station and 1.5 m above the floor.

The beampattern measurement strategy is demonstrated in Fig. 3(c) in which the beampattern measurement apparatus will measure the signal power every 18 degrees with a radius of 2 m. Therefore, it will measure 10 points considering 180 degrees. To ensure accurate measurement, the beampattern measurement apparatus is placed at the same height with the base station antenna array. It should be noted that the experiment platform employs small dipole antennas for signal transmission. The size of each dipole antenna is similar to one wavelength λ when considering the carrier frequency f_{RF}=2.4 GHz. Therefore, the beampattern measurement at a 2 m distance is greater than 2λ [48] and is practically within the far-field range. In addition, to mitigate multipath effect to the beampattern measurement, we use a 6 dBi LP PCB antenna, which has a narrow and focused radiation beam. Therefore, it can focus on the LOS signal collection

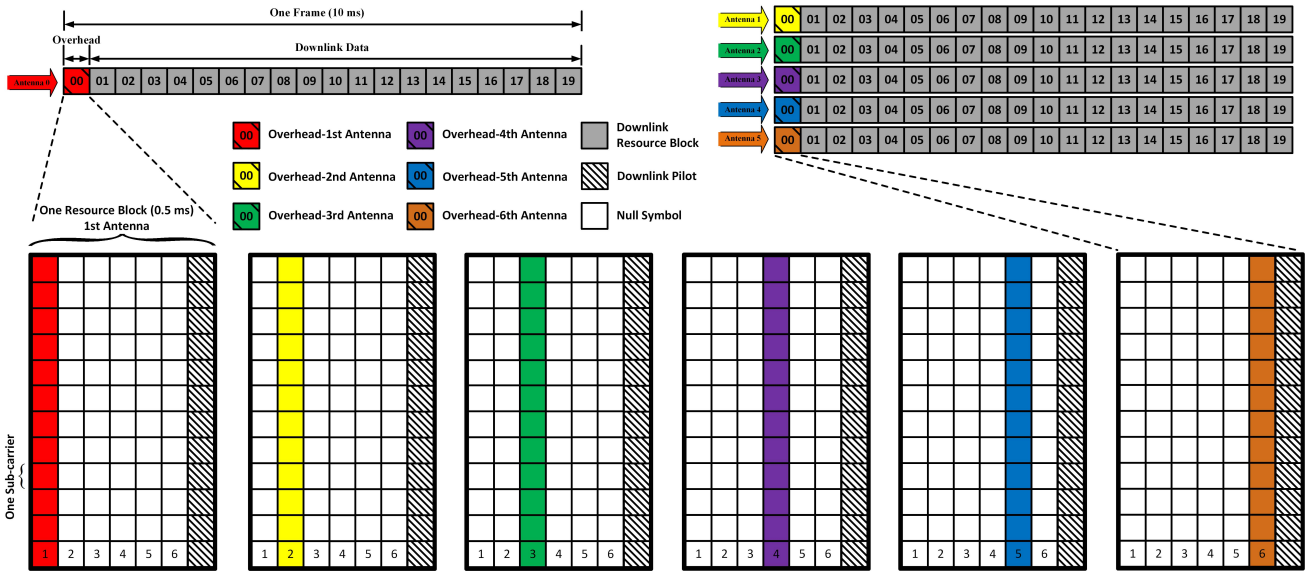

FIGURE 4. Frame and resource block structure for the dual-functional sensing and communication multiuser MIMO signal.

within its beam range and avoid potential multipath signal collections from other reflection directions. For the sensing part, we have a stand-alone RF chain in a USRP for the beampattern power measurement.

The beampattern power computation is based on received symbols. Since each symbol has real and imaginary parts, therefore the power will be calculated as

$$P = \frac{1}{Q}\sum_{k=1}^{Q}\left[\Re(x_k)^2 + \Im(x_k)^2\right], \tag{14}$$

where x_k indicates the k^{th} received complex symbol and $\frac{1}{Q}$ is the scaling factor for average power computation. $\Re(\cdot)$ and $\Im(\cdot)$ indicate the real part and imaginary part of a symbol, respectively.

C. FRAME DESIGN AND CHANNEL ESTIMATION

1) FRAME STRUCTURE

The frame structure for this experiment follows the 3GPP standardized 4G requirement [5] and reused from [42]. The frame structure is shown in Fig. 4 where 20 resource blocks are combined to form one frame. The time duration for one frame is 10 ms. We consider an indoor channel environment with slow channel variations, therefore the first resource block is reserved for signalling overhead, which will be used mainly for MIMO channel estimation. In this case, the MIMO precoding is only operated once every 20 resource blocks, which greatly reduces signal precoding complexity. Each resource block includes seven OFDM symbols and the first resource block has a unique OFDM symbol allocation scheme. The interference from MIMO antennas can be solved via transmitter precoding based on estimated CSI, which indicates the importance of accurate CSI estimation. To avoid interference to CSI estimation, we multiplex the overhead at each antenna in time-domain as illustrated in Fig. 4. In this case, even though the data part is interfered, the overhead part is interference free. It should be noted that to mitigate potential channel and hardware imperfections, an additional downlink pilot is applied for all the data streams.

2) MIMO CHANNEL ESTIMATION

Based on the interleaved overhead structure in Fig. 4, we define a pilot matrix as

$$\mathbf{P} = \begin{bmatrix} p_1 & 0 & 0 & 0 & 0 & 0 \\ 0 & p_2 & 0 & 0 & 0 & 0 \\ 0 & 0 & p_3 & 0 & 0 & 0 \\ 0 & 0 & 0 & p_4 & 0 & 0 \\ 0 & 0 & 0 & 0 & p_5 & 0 \\ 0 & 0 & 0 & 0 & 0 & p_6 \end{bmatrix}, \tag{15}$$

where $p_1, p_2, p_3, p_4, p_5, p_6$ are one pilot symbol at each antenna.

The system is in a 2×6 channel model with the matrix format as

$$\mathbf{H} = \begin{bmatrix} h_{11} & h_{12} & h_{13} & h_{14} & h_{15} & h_{16} \\ h_{21} & h_{22} & h_{23} & h_{24} & h_{25} & h_{26} \end{bmatrix}. \tag{16}$$

Therefore, after the MIMO channel and additive white Gaussian noise (AWGN) contamination, the received symbol matrix is expressed as

$$\begin{bmatrix} y_{11} & y_{12} & y_{13} & y_{14} & y_{15} & y_{16} \\ y_{21} & y_{22} & y_{23} & y_{24} & y_{25} & y_{26} \end{bmatrix} = \mathbf{HP} + \begin{bmatrix} z_{11} & z_{21} \\ z_{12} & z_{22} \\ z_{13} & z_{23} \\ z_{14} & z_{24} \\ z_{15} & z_{25} \\ z_{16} & z_{26} \end{bmatrix}^T, \tag{17}$$

where $y_{m,n}$ indicates the received symbols at the m^{th} user from the n^{th} antenna. Therefore, the MIMO channel matrix

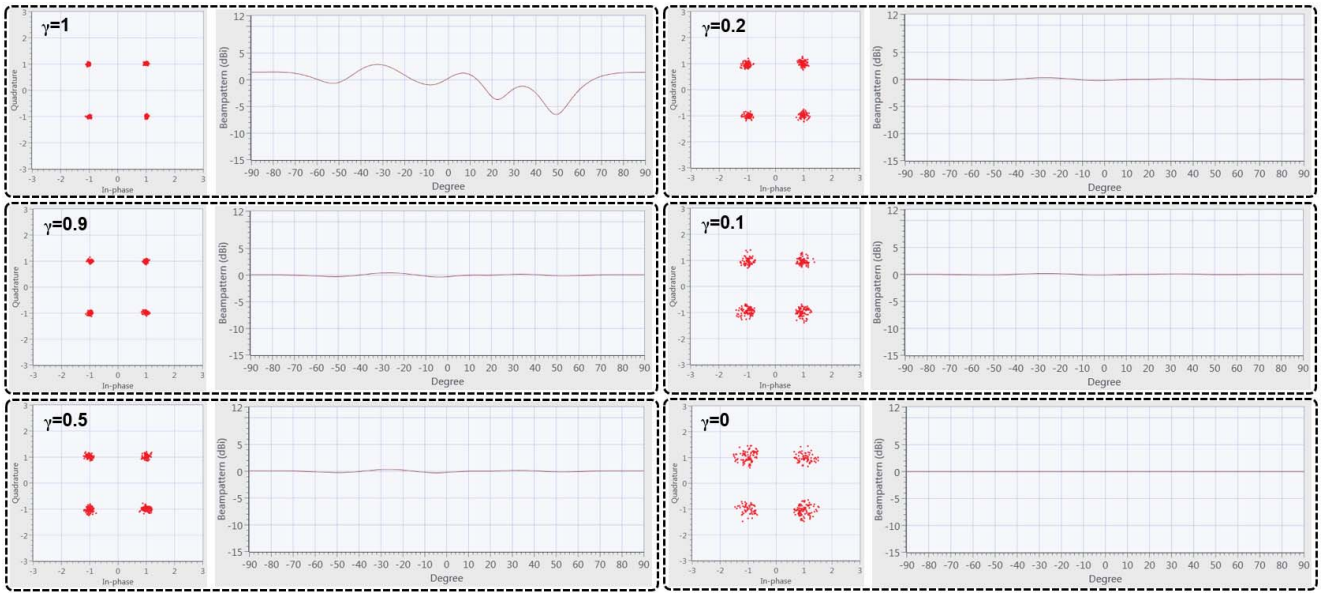

FIGURE 5. Experiment results in user side constellation diagram measurements and Tx-USRP side omnidirectional beampatterns.

can be calculated regardless of noise via

$$\hat{\mathbf{H}} = \begin{bmatrix} y_{11}/p_1 & y_{12}/p_2 & y_{13}/p_3 & y_{14}/p_4 & y_{15}/p_5 & y_{16}/p_6 \\ y_{21}/p_1 & y_{22}/p_2 & y_{23}/p_3 & y_{24}/p_4 & y_{25}/p_5 & y_{26}/p_6 \end{bmatrix}. \tag{18}$$

Based on the estimated MIMO channel matrix $\hat{\mathbf{H}}$, the Tx-USRP Array can do signal precoding such that MIMO antenna interference can be avoided.

3) OFDM CHANNEL ESTIMATION

Multicarrier signals can effectively convert a multipath effect into an equivalent diagonal composite matrix due to the use of Fourier transform. Unlike the MIMO channel matrix $\mathbf{H}$, we define a new channel matrix $\mathbf{G}$ for the multipath effect. Following the AWGN channel distorted signal expression in (6), the new expression considering multipath is give by

$$\mathbf{y} = \mathbf{GFp}_g + \mathbf{z}, \tag{19}$$

where $\mathbf{p}_g$ is the downlink pilot symbol defined in Fig. 4.

After demodulation at the receiver, the distorted signal is expressed as

$$\mathbf{r}_g = \mathbf{F}^*\mathbf{GFp}_g + \mathbf{F}^*\mathbf{z} = \mathbf{Dp}_g + \mathbf{w}_z, \tag{20}$$

where $\mathbf{D}$=$\mathbf{F}^*\mathbf{GF}$ is an diagonal matrix, in which its diagonal elements *diag*($\mathbf{D}$) can be extracted for one-tap equalization such that multipath, imperfect timing, phase offset and power distortion will be removed.

D. EXPERIMENT RESULTS

We practically verify the trade-off between communications and sensing functions. The Tx-USRP Array, two receiver side users and the beampattern measurement apparatus are placed following the floor plan in Fig. 3(a). At the beginning, we will not add AWGN to the testbed and just check the functionality of the communication part and sensing part. To evaluate the trade-off between communication and beampattern, we test different representative values for γ such as γ=1, 0.9, 0.5, 0.2, 0.1, 0.

The measured results for omnidirectional systems are shown in Fig. 5 where different values of γ are configured. In this result, we plot the theoretical transmitter side beampattern from Tx-USRP Array based on the estimated MIMO channel matrix in (18). Since the measurement at this point is not affected by over-the-air multipath, its beampattern can be used as a benchmark for practical beampattern measurement. It is observed that small values of γ will degrade communication performance evidenced by the fact that the constellation points are more scattered. However, the beampattern becomes better when the value of γ reduces. With the increase of γ, constellation points are more focused leading to potentially better BER performance but at the cost of more distorted beampatterns. Accordingly, it is clear that there is a trade-off configuration between communication performance and beampattern quality. Based on the observation in Fig. 5, it is obvious that when γ is large sufficient, it will provide a pure communication achievable waveform. The trade-off value can be reduced to γ=0.9 such that constellation points are clearly separated while the beampattern is still roughly in a perfect beampattern shape.

For the directional system measurement illustrated in Fig. 6, its trade-off variation is more obvious. When γ=0.2, 0.1, 0, the communication is greatly degraded since constellation points are scattered and rotated. However, the above systems show high quality beampatterns. When γ is increased to 0.5, constellation points start to appear. Further increasing γ to 0.9, the constellation becomes even better with a reasonable beampattern. Therefore, similar to the omnidirectional results in Fig. 5, γ=0.9 can be thought of

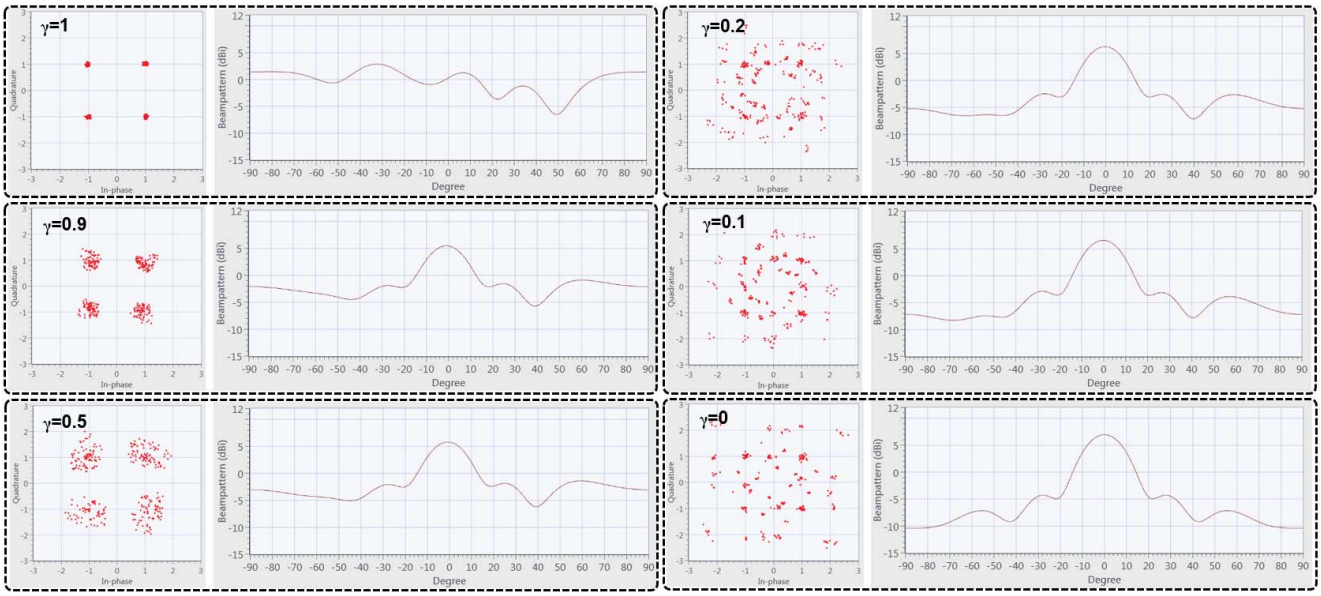

FIGURE 6. Experiment results in user side constellation diagram measurements and Tx-USRP side directional beampatterns.

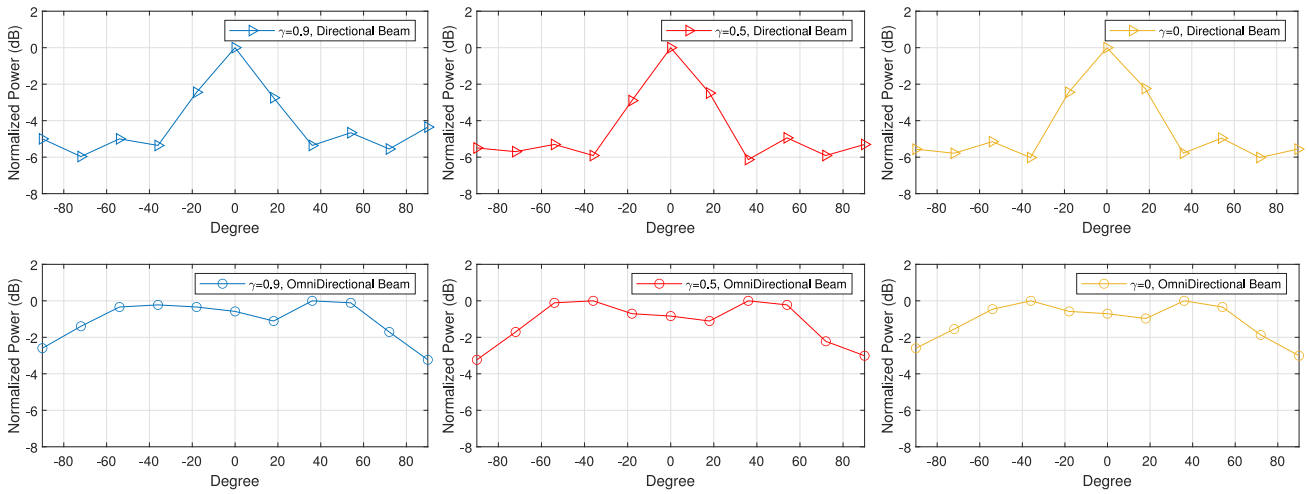

FIGURE 7. Measured Omnidirectional and directional beampatterns when γ=0.9, 0.5, 0.

as a desirable setup for directional sensing where still a clear beam is obtained with a peak to side lobe ratio (PSLR) of 6 dB. It is noted that γ=1 indicates pure communication systems. Therefore, the obtained beampatterns for the directional and omnidirectional design in Fig. 5 and Fig. 6 are identical.

Beampatterns are measured and included in Fig. 7 where it is obvious that the three directional beampatterns show peaks at θ=0° while all other angles have lower normalized power. In this case, a directional beampattern is obtained and it is in good agreement with the ideal pattern at Tx-USRP Array in Fig. 6, but with a reduced PSLR of about 4 dB. For the omnidirectional beampattern measured in Fig. 7, the measured patterns are not flat as expected from Fig. 5 but are within 3 dB. It should be noted that the aim of the ISAC beam in this work is to detect activity based on power measurement while channel estimation aims to compute CSI based on pilot symbols. In our current experiment, we only measure beam power and therefore the sensing beam cannot be used for channel estimation. However, once we can recover the data from the ISAC beam, it can be used for channel estimation.

Constellation diagram is a visual way to tell the performance of communications. Fig. 8 compares constellation performance in terms of EVM for omnidirectional and directional ISAC systems under different values of γ. As expected, the EVM for both omnidirectional and directional systems becomes better with the increase of γ. In addition, the EVM of omnidirectional systems outperforms directional systems at all values of γ. Moreover, it is observed that the variations of γ have smooth impact on omnidirectional communication systems while its value changing has great effect

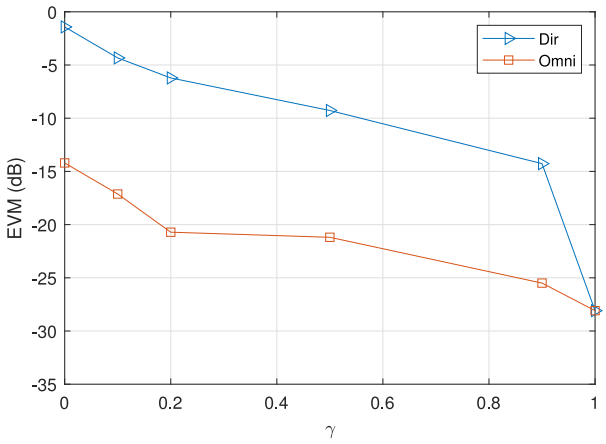

FIGURE 8. Measured EVM versus γ for omnidirectional (Omni) and directional (Dir) ISAC systems.

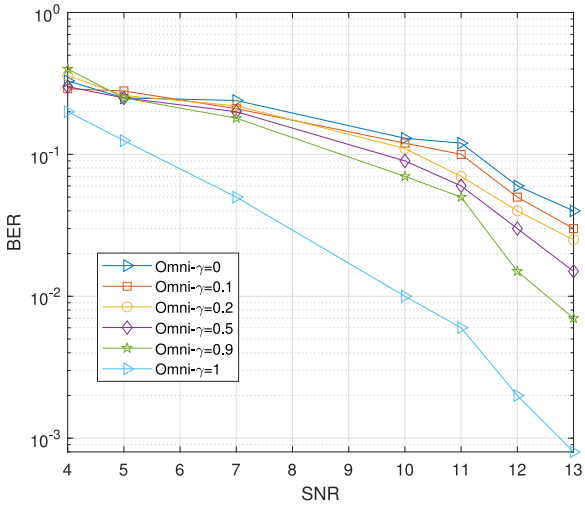

FIGURE 9. Experiment BER measurement for different omnidirectional (Omni) systems.

on directional communication systems especially when the value of γ is between 0.9 and 1. The above discoveries can be explained based on the observations from Fig. 5 and Fig. 6.

For a complete BER versus SNR measurement, we maintain the total transmission signal power and tune noise power such that various SNRs can be obtained. Fig. 9 demonstrates the measured BER for omnidirectional systems. It is clear that the pure sensing scenario corresponding to γ=0 exhibits the worst BER performance when γ=0. The pure communication scenario shows the best performance when γ=1. All other values of $0 < \gamma < 1$ show a trade-off between the BER performance and the beampattern quality. As explained before, for γ=0.9 there is approximately 2-3 dB gap with the pure communication system when γ=1. Jointly considering the measured beampattern of γ=0.9 in Fig. 7, it is inferred that an ISAC system can realize dual functional communications and sensing at the cost of BER performance loss. BER variations for directional systems are more obvious in

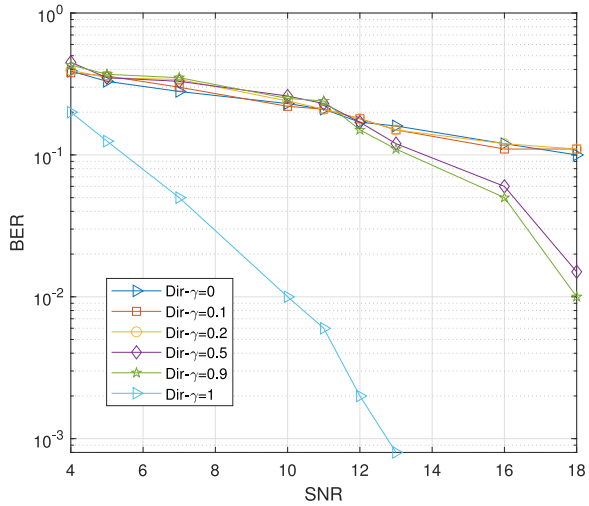

FIGURE 10. Experiment BER measurement for different directional (Dir) systems.

Fig. 10 where the performance gap between γ=1 and γ=0.9 is increased to around 8 dB. The reason can be observed by constellations in Fig. 6 and EVM in Fig. 8

VI. SENSING APPLICATION USING THE TESTBED

In this section we present an elementary experiment to validate the sensing performance of the ISAC design. We note that our indoor facilities, limited by signal carrier frequency, bandwidth and receiver antennas, do not allow for a classical radar angle-range-Doppler estimation for the given operational frequency of our testbed. The antenna array is configured at the transmitter side rather than the receiver side, and therefore it cannot accurately measure angle of reflected signals. Moreover, the initial objective of our ISAC experiment is not for traditional radar detection but for an activity detection scenario as shown in Fig. 11(a) using the directional beam demonstrated in the previous section. The aim is, employing the directional beam from our designed ISAC waveform, to detect the presence of an obstacle. We use this setup to emulate the detection of a person crossing the directional beam. The application itself doesn't need to know the target distance and velocity. The application can only be achieved by our proposed waveform since traditional designs cannot support multiuser MIMO communication and directional sensing at the same time. In particular we use an radiation absorbent material as an obstacle to emulate the presence of a person, and measure the received power over the direction of the sensing beam for the different positions of the obstacle between Locations Lo-A to Lo-E in Fig. 11(d).

The floor plan of the measurement setup is demonstrated in Fig. 11(d) where the Tx-USRP Array, CU-1, CU-2 and Ant are placed in fixed locations. We merely change the object locations and place the object in five different locations in Fig. 11(d) and operate five separate measurements.

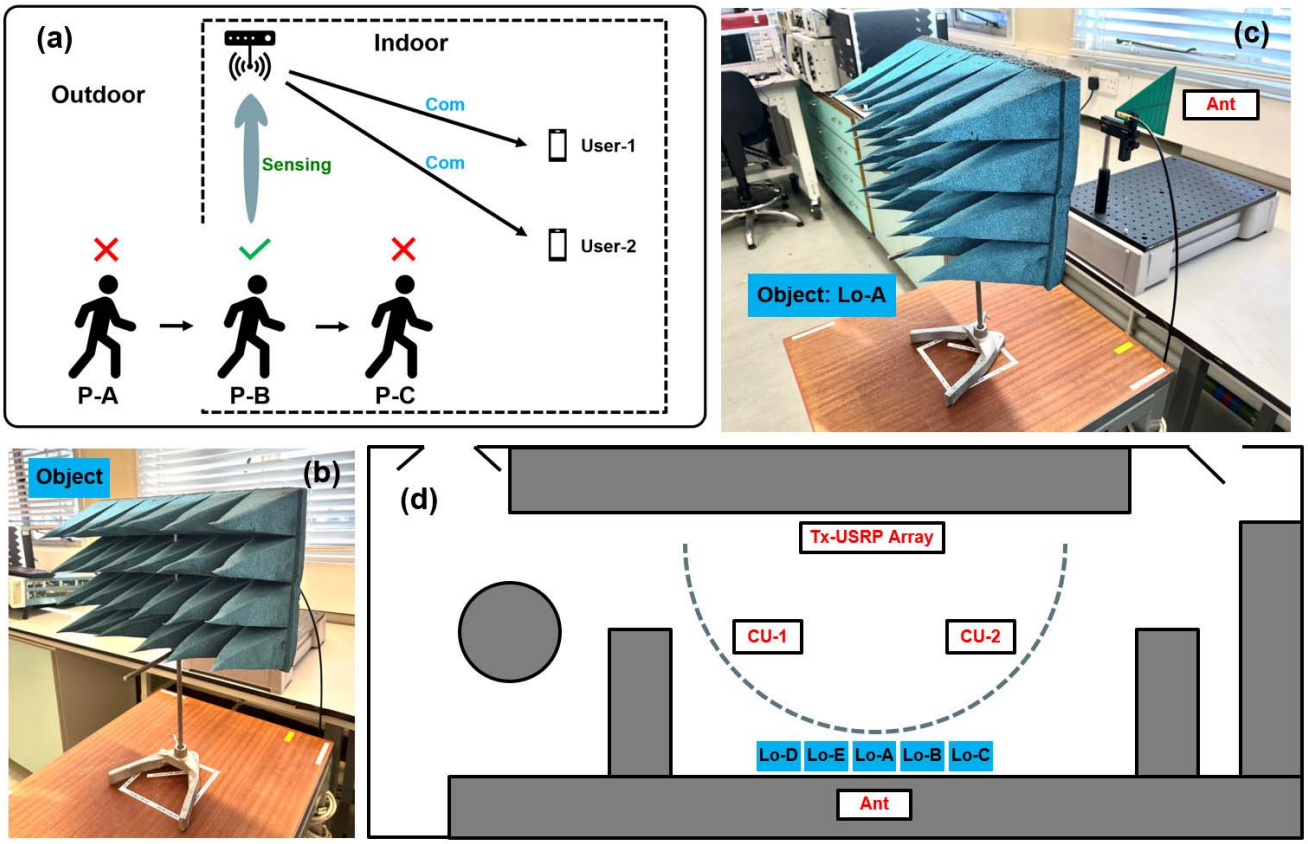

FIGURE 11. Indoor people counting application scenario using the ISAC experiment setup. (a) Proposed people counting scenario. The ISAC transmitter is placed at the top aiming to work vertically. However, the ISAC transmitter placement is flexible and it can work horizontally as well. (b) The object used to emulate a person in the experiment. (c) The placement of the object at Lo-A as one example. (d) Indoor experiment setup floor plan.

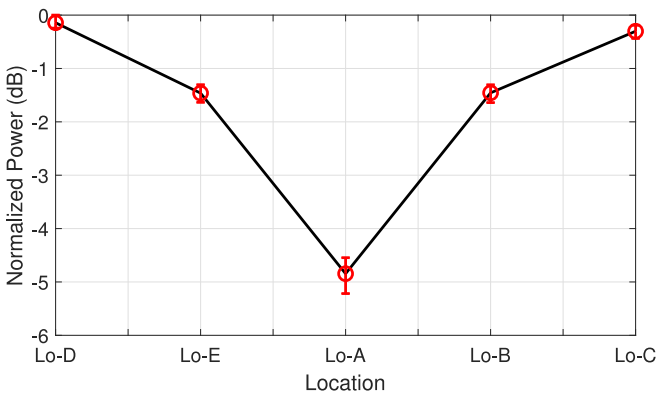

FIGURE 12. Normalized power measurement with error bars at each location when ISAC based multiuser-MIMO system is deployed.

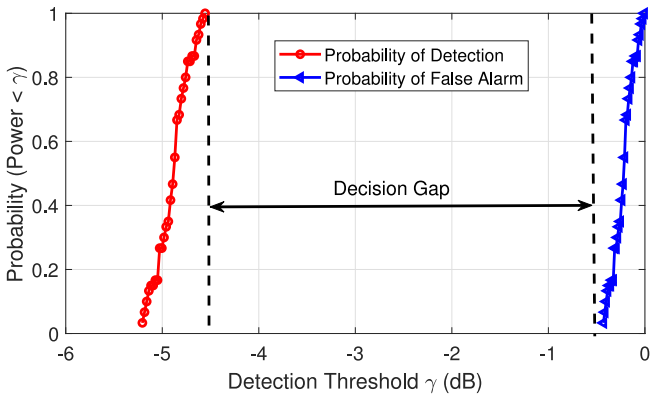

FIGURE 13. Detection probability.

The normalized power measurement at five locations is illustrated in Fig. 12, in which it is obvious that the power measured at location Lo-A, when the emulated obstacle is blocking the sensing beam, is greatly degraded compared to the power measured from other locations. The deviation of the measured power in the different locations is shown by the red bars in the figure. Beneficially, since the ISAC waveform in this work can steer a directional beam towards a location, therefore the error bar computed at one location would not overlap with others from adjacent locations. Accordingly, using the power levels in Fig. 12 and applying a simple detection threshold, we can detect the presence of the obstacle in a directional beam, i.e., detect a person crossing the beam.

Detection probability is also plotted in Fig. 13 where the probability of detection P_D and the false alarm probability P_{FA} are defined by

$$P_D = Pr(\textit{received power} \leq \gamma | \textit{obstacle presence}), \quad (21)$$

$$P_{FA} = Pr(\textit{received power } \leq \gamma | \textit{obstacle absence}), \quad (22)$$

We can emulate the detection probability using the measurements for Lo-A, and the false alarm probability using Lo-C and Lo-D. Since the directional beam is robust to environment variations outside location Lo-A, Fig. 13 shows that the experiment testbed can accurately detect the existence of the object with a 4 dB gap achieved between true detection and false alarm. Accordingly, between our communication BER results in Fig. 9 and Fig. 10, and our sensing results in Fig. 12 and Fig. 13, this experiment has demonstrated the dual functionality of the presented transmission scheme.

VII. CONCLUSION

This work designed an over-the-air multi-user MIMO-OFDM testbed to validate a dual-functional sensing and communication waveform. Over-the-air experiments reveal a graceful trade-off between the performance for both sensing and communication functions. Practical measured sensing beampatterns have reasonable radiation shape compared to simulation results. The BER results demonstrate a performance degradation of 2.5 dB relative to pure communications when omnidirectional radiation waveform is applied while the performance loss is widened to 8 dB when a directional radiation waveform is used. In terms of sensing functionality, the ISAC beam can correctly detect activity variations with a 4 dB protective decision gap. The successful experimental validation of the trade-off between communication and sensing performance using the dual-functional ISAC waveform can boost the future research on new communication waveform and sensing beampattern design.

REFERENCES

[1] T. Rappaport, R. Heath, R. Daniels, and J. Murdock, *Millimeter Wave Wireless Communications*. Upper Saddle River, NJ, USA: Prentice-Hall, 2014.

[2] H.-J. Song and T. Nagatsuma, "Present and future of terahertz communications," *IEEE Trans. THz Sci. Technol.*, vol. 1, no. 1, pp. 256–263, Sep. 2011.

[3] E. G. Larsson, O. Edfors, F. Tufvesson, and T. L. Marzetta, "Massive MIMO for next generation wireless systems," *IEEE Commun. Mag.*, vol. 52, no. 2, pp. 186–195, Feb. 2014.

[4] E. Dahlman, S. Parkvall, J. Sköld, and P. Beming, *3G Evolution: HSPA and LTE for Mobile Broadband*. Oxford, U.K.: Elsevier, 2007.

[5] E. Dahlman, S. Parkvall, and J. Sköld, *4G LTE/LTE-Advanced for Mobile Broadband*. Amsterdam, The Netherlands: Elsevier, 2011.

[6] E. Dahlman, S. Parkvall, and J. Sköld, *5G NR: The Next Generation Wireless Access Technology*. Amsterdam, The Netherlands: Academic, 2018.

[7] T. Xu and I. Darwazeh, "Transmission experiment of bandwidth compressed carrier aggregation in a realistic fading channel," *IEEE Trans. Veh. Technol.*, vol. 66, no. 5, pp. 4087–4097, May 2017.

[8] J. Anderson, F. Rusek, and V. Öwall, "Faster-than-Nyquist signaling," *Proc. IEEE*, vol. 101, no. 8, pp. 1817–1830, Aug. 2013.

[9] Y. Ma, N. Wu, J. A. Zhang, B. Li, and L. Hanzo, "Parametric bilinear iterative generalized approximate message passing reception of FTN multi-carrier signaling," *IEEE Trans. Commun.*, vol. 69, no. 12, pp. 8443–8458, Dec. 2021.

[10] R. Hadani *et al.*, "Orthogonal time frequency space modulation," in *Proc. IEEE Wireless Commun. Netw. Conf. (WCNC)*, 2017, pp. 1–6.

[11] N. Wu, Y. Zhang, Y. Ma, B. Li, and W. Yuan, "Vector approximate message passing based iterative receiver for OTFS system," in *Proc. IEEE/CIC Int. Conf. Commun. China (ICCC Workshops)*, 2021, pp. 422–426.

[12] N. Michailow *et al.*, "Generalized frequency division multiplexing for 5th generation cellular networks," *IEEE Trans. Commun.*, vol. 62, no. 9, pp. 3045–3061, Sep. 2014.

[13] B. Farhang-Boroujeny, "OFDM versus filter bank multicarrier," *IEEE Signal Process. Mag.*, vol. 28, no. 3, pp. 92–112, May 2011.

[14] J. Lien *et al.*, "Soli: Ubiquitous gesture sensing with millimeter wave radar," *ACM Trans. Graph.*, vol. 35, no. 4, p. 142, Jul. 2016.

[15] S. Z. Gurbuz, C. Clemente, A. Balleri, and J. J. Soraghan, "micro-doppler-based in-home aided and unaided walking recognition with multiple radar and sonar systems," *IET Radar Sonar Navigation*, vol. 11, no. 1, pp. 107–115, 2017.

[16] V. Chen, F. Li, S.-S. Ho, and H. Wechsler, "Micro-doppler effect in radar: Phenomenon, model, and simulation study," *IEEE Trans. Aerosp. Electron. Syst.*, vol. 42, no. 1, pp. 2–21, Jan. 2006.

[17] G. Zhang, H. Li, and F. Wenger, "Object detection and 3D estimation via an FMCW radar using a fully convolutional network," in *Proc. IEEE Int. Conf. Acoust., Speech Signal Process. (ICASSP)*, 2020, pp. 4487–4491.

[18] Z. Hu *et al.*, "Design and analysis of a UWB MIMO radar system with Miniaturized Vivaldi antenna for through-wall imaging," *Remote Sens.*, vol. 11, no. 16, p. 1867, 2019.

[19] F. Adib and D. Katabi, *See Through Walls With WiFi!* New York, NY, USA: Assoc. Comput. Mach., 2013.

[20] "IEEE 802.11bf task group (TG): Status of project IEEE 802.11bf." 2021. [Online]. Available: https://www.ieee802.org/11/Reports/tgbf_update.htm

[21] O. Kaltiokallio, H. Yigitler, R. Jäntti, and N. Patwari, "Non-invasive respiration rate monitoring using a single COTS TX-RX pair," in *Proc. 13th Int. Symp. Inf. Process. Sens. Netw.*, 2014, pp. 59–69.

[22] N. Patwari, L. Brewer, Q. Tate, O. Kaltiokallio, and M. Bocca, "Breathfinding: A wireless network that monitors and locates breathing in a home," *IEEE J. Sel. Topics Signal Process.*, vol. 8, no. 1, pp. 30–42, Feb. 2014.

[23] H. Abdelnasser, K. A. Harras, and M. Youssef, "UbiBreathe: A ubiquitous non-invasive WiFi-based breathing estimator," 2015, *arXiv:1505.02388*.

[24] Z. Yang, P. H. Pathak, Y. Zeng, X. Liran, and P. Mohapatra, "Monitoring vital signs using millimeter wave," in *Proc. MobiHoc*, 2016, pp. 211–220.

[25] G. Z. Y. Ma and S. Wang, "WiFi sensing with channel state information: A survey," *ACM Comput. Surveys*, vol. 52, no. 3, pp. 1–36, 2019.

[26] Q. Song, S. Guo, X. Liu, and Y. Yang, "CSI amplitude fingerprinting-based NB-IoT indoor localization," *IEEE Internet Things J.*, vol. 5, no. 3, pp. 1494–1504, Jun. 2018.

[27] C. Wu, Z. Yang, Z. Zhou, K. Qian, Y. Liu, and M. Liu, "PhaseU: Real-time LOS identification with WiFi," in *Proc. IEEE Conf. Comput. Commun. (INFOCOM)*, 2015, pp. 2038–2046.

[28] X. Wang, C. Yang, and S. Mao, "PhaseBeat: Exploiting CSI phase data for vital sign monitoring with commodity WiFi devices," in *Proc. IEEE 37th Int. Conf. Distrib. Comput. Syst. (ICDCS)*, 2017, pp. 1230–1239.

[29] Y. Wang, K. Wu, and L. M. Ni, "WiFall: Device-free fall detection by wireless networks," *IEEE Trans. Mobile Comput.*, vol. 16, no. 2, pp. 581–594, Feb. 2017.

[30] G. Wang, Y. Zou, Z. Zhou, K. Wu, and L. M. Ni, "We can hear you with Wi-Fi!" *IEEE Trans. Mobile Comput.*, vol. 15, no. 11, pp. 2907–2920, Nov. 2016.

[31] K. Qian, C. Wu, Z. Yang, Y. Liu, F. He, and T. Xing, "Enabling contactless detection of moving humans with dynamic speeds using CSI," *ACM Trans. Embedded Comput. Syst.*, vol. 17, no. 2, p. 52, Jan. 2018.

[32] J. Liu, Y. Chen, Y. Wang, X. Chen, J. Cheng, and J. Yang, "Monitoring vital signs and postures during sleep using WiFi signals," *IEEE Internet Things J.*, vol. 5, no. 3, pp. 2071–2084, Jun. 2018.

[33] Q. Zhang, H. Sun, Z. Wei, and Z. Feng, "Sensing and communication integrated system for autonomous driving vehicles," in *Proc. IEEE Conf. Comput. Commun. Workshops (INFOCOM WKSHPS)*, 2020, pp. 1278–1279.

[34] P. M. McCormick, S. D. Blunt, and J. G. Metcalf, "Simultaneous radar and communications emissions from a common aperture, part I: Theory," in *Proc. IEEE Radar Conf. (RadarConf)*, 2017, pp. 1685–1690.

[35] P. M. McCormick, B. Ravenscroft, S. D. Blunt, A. J. Duly, and J. G. Metcalf, "Simultaneous radar and communication emissions from a common aperture, part II: Experimentation," in *Proc. IEEE Radar Conf. (RadarConf)*, 2017, pp. 1697–1702.

[36] J. B. Sanson, D. Castanheira, A. Gameiro, and P. P. Monteiro, "Non-orthogonal multicarrier waveform for radar with communications systems: 24 GHz GFDM RadCom," *IEEE Access*, vol. 7, pp. 128694–128705, 2019.

[37] J. Wang, X.-D. Liang, L.-Y. Chen, L.-N. Wang, and K. Li, "First demonstration of joint wireless communication and high-resolution SAR imaging using airborne MIMO radar system," *IEEE Trans. Geosci. Remote Sens.*, vol. 57, no. 9, pp. 6619–6632, Sep. 2019.

[38] C. B. Barneto *et al.*, "Full-duplex OFDM radar with LTE and 5G NR waveforms: Challenges, solutions, and measurements," *IEEE Trans. Microw. Theory Techn.*, vol. 67, no. 10, pp. 4042–4054, Oct. 2019.

[39] P. Kumari, A. Mezghani, and R. W. Heath, "JCR70: A low-complexity Millimeter-wave proof-of-concept platform for a fully-digital SIMO joint communication-radar," *IEEE Open J. Veh. Technol.*, vol. 2, pp. 218–234, 2021.

[40] T. Huang, N. Shlezinger, X. Xu, Y. Liu, and Y. C. Eldar, "MAJoRCom: A dual-function radar communication system using index modulation," *IEEE Trans. Signal Process.*, vol. 68, pp. 3423–3438, 2020, doi: 10.1109/TSP.2020.2994394.

[41] F. Liu, L. Zhou, C. Masouros, A. Li, W. Luo, and A. Petropulu, "Toward dual-functional radar-communication systems: Optimal waveform design," *IEEE Trans. Signal Process.*, vol. 66, no. 16, pp. 4264–4279, Aug. 2018.

[42] T. Xu, C. Masouros, and I. Darwazeh, "Waveform and space precoding for next generation downlink narrowband IoT," *IEEE Internet Things J.*, vol. 6, no. 3, pp. 5097–5107, Jun. 2019.

[43] F. Liu *et al.*, "Integrated sensing and communications: Towards dual-functional wireless networks for 6G and beyond," 2021, *arXiv:2108.07165*.

[44] D. R. Fuhrmann and G. S. Antonio, "Transmit beamforming for MIMO radar systems using signal cross-correlation," *IEEE Trans. Aerosp. Electron. Syst.*, vol. 44, no. 1, pp. 171–186, Jan. 2008.

[45] P. Stoica, J. Li, and Y. Xie, "On probing signal design for MIMO radar," *IEEE Trans. Signal Process.*, vol. 55, no. 8, pp. 4151–4161, Aug. 2007.

[46] "LPS-402 programmable phase shifter." Vaunix. May 2019. [Online]. Available: https://vaunix.com/lps-402-digital-phase-shifter/

[47] T. Xu, C. Masouros, and I. Darwazeh, "Design and prototyping of hybrid analogue digital multiuser MIMO beamforming for non-orthogonal signals," *IEEE Internet Things J.*, vol. 7, no. 3, pp. 1872–1883, Mar. 2020.

[48] C. A. Balanis, *Antenna Theory—Analysis and Design*. Hoboken, NJ, USA: Wiley, 2016. [Online]. Available: https://app.knovel.com/hotlink/toc/id:kpATADE01N/antenna-theory-analysis/antenna-theory-analysis